

Simultaneous seeing measurement through the Subaru Telescope in the visible and near-infrared bands for the wavelength dependence evaluation

Shin Oya¹ · Hiroshi Terada² · Yutaka Hayano³ ·
Makoto Watanabe⁴ · Masayuki Hattori⁵ ·
Yosuke Minowa⁶

Received: 17 January 2016 / Accepted: 23 May 2016 / Published online: 13 July 2016
© Springer Science+Business Media Dordrecht 2016

Abstract Stellar images have been obtained under natural seeing at visible and near-infrared wavelengths simultaneously through the Subaru Telescope at Mauna Kea. The image quality is evaluated by the full-width at the half-maximum (FWHM) of the stellar images. The observed ratio of FWHM in the *V*-band to the *K*-band is 1.54 ± 0.17 on average. The ratio shows tendency to decrease toward bad seeing as expected from the outer scale influence, though the number of the samples is still limited. The ratio is important for simulations to evaluate the performance of a ground-layer adaptive optics system at near-infrared wavelengths based on optical seeing statistics. The observed optical seeing is also compared with outside seeing to estimate the dome seeing of the Subaru Telescope.

✉ Shin Oya
shin.oya@nao.ac.jp

- ¹ TMT-J Project Office, National Astronomical Observatory of Japan, 2-21-1 Osawa, Mitaka, Tokyo 181-8588, Japan
- ² Thirty Meter Telescope Project, National Astronomical Observatory of Japan, 100 West Walnut, Suite 300, Pasadena, CA 91124, USA
- ³ Advanced Technology Center / TMT-J Project Office, National Astronomical Observatory of Japan, 2-21-1 Osawa, Mitaka, Tokyo 181-8588, Japan
- ⁴ Department of Applied Physics, Okayama University of Science, 1-1 Ridai-cho, Kita-ku, Okayama, Okayama 700-0005, Japan
- ⁵ Spectrography and Bioimaging Facility, National Institute for Basic Biology, Nishigonaka 38, Myodaiji, Okazaki, Aichi 444-8585, Japan
- ⁶ Subaru Telescope, 650 North Aohoku Pl., Hilo, HI 96720, USA

Keywords Seeing · Visible · Near-infrared · Adaptive optics · Outer scale

1 Introduction

It is known that the wavelength dependence of image quality varies with atmospheric conditions. The optical image quality in terms of spatial resolution is commonly evaluated by the full-width at the half maximum (FWHM) of a point-source, called 'seeing'. The seeing size is in inverse proportion of the spatial-correlation length of the atmospheric turbulence, r_0 (Fried parameter, [1]). Usually, r_0 is measured at visible wavelength ($0.5 \mu\text{m}$) by, for example, differential image motion monitor (DIMM, e.g., [2]). Thus, the most of long-term statistics are also provided at the visible wavelength. When the statistics in the infrared wavelength are needed, the visible seeing size must be converted into the infrared wavelengths. The conversion factor (the ratio of the visible FWHM to the infrared FWHM) is determined by the wavelength dependence of r_0 . In the case of Kolmogorov turbulence, r_0 changes with the wavelength λ as $r_0 \propto \lambda^{6/5}$ (e.g., Tab2.1 in [3]). However, the dependence of r_0 varies with the outer scale, L_0 , in the power spectrum of more realistic von Kármán turbulence even for the same r_0 [4, 5].

The variation of the conversion factor must be taken into account for the performance simulation of adaptive optics (AO) systems at infrared wavelengths, based on the visible seeing statistics. This is quite important, especially in the case of ground-layer AO (GLAO, [6, 7]) which is a candidate of the next-generation AO system at Subaru Telescope¹ in combination with a wide-field infrared instrument (ULTIMATE-SUBARU, [8]). GLAO improves the seeing size over a wide field-of-view (FoV) rather than achieves the diffraction limit in a narrow FoV, because only the turbulence close to the ground level is corrected and the uncorrected upper atmospheric turbulence determines the image quality [6, 9]. Therefore, the performance of GLAO is evaluated by the ratio of the image size corrected by GLAO to the seeing (uncorrected) image size. For correct estimation of the GLAO benefit at the near infrared wavelengths, the seeing image size at the same wavelength is needed. Usually, the seeing condition (r_0) of a simulation is specified at the visible wavelength ($0.5 \mu\text{m}$) based on long term seeing statistics even for calculating the AO-corrected image at near infrared wavelengths. Because the seeing at the near infrared wavelengths changes with the outer scale even with the same visible seeing condition, the value of outer scale in a simulation must be selected to reproduce the observed ratio of image size in the near infrared bands to the optical. Typical outer scale of 30 m is often adopted as a standard value in simulations for AO systems (e.g., [9, 10]) including those of Subaru Telescope [11–13], and it is within consistent range of a field measurement at Mauna Kea [14].

In this paper, we present simultaneously observed ratio of the seeing in the *V*-band ($0.55 \mu\text{m}$) to that in the *K*-band ($2.2 \mu\text{m}$) through the Subaru Telescope to evaluate the conversion factor between the visible and infrared seeing. The information is

¹<http://www.naoj.org/>.

Table 1 Catalog data of the stars used for the observation

Star ID	USNO-B1.0	2MASS	<i>B</i>	(<i>V</i>)	<i>R</i>	<i>K</i>
1	0891-0055324	J05085235–0053171	10.4	(10.1)	9.9	9.4
2	0888-0186231	J09435307–0110162	10.4	(10.2)	10.0	9.2
3	0899-0215891	J12562701–0000297	13.6	—	12.6	11.1
4	0908-0486357	J19593956+0048112	10.7	(10.5)	10.2	9.1
5	0845-0235662	J12422937–0526498	10.4	(10.2)	10.0	8.7
6	0812-0248578	J12410046–0845223	10.0	(9.8)	9.6	8.9
7	0846-0234421	J12352590–0519215	10.5	(10.1)	9.6	8.3
8	0835-0235801	J12431896–0624503	11.7	—	9.9	7.0
9	0840-0239864	J12531020–0557400	10.9	(10.3)	9.7	8.1
10	0831-0288025	J12574065–0653524	10.9	(10.3)	9.8	7.9

important to validate the improvement of the image size in the Subaru GLAO simulation [12, 13]. The *K*-band images were obtained by an AO assisted infrared camera and the *V*-band images were acquired by a visible camera in the AO system itself. The use of AO just before the seeing measurement is helpful to cancel the drift of the telescope focus caused by the temperature change. Because the typical outer scale size is close to the aperture size of Subaru Telescope, the influence of the outer scale is expected to be clearly seen as the ratio of the seeing size in the simultaneously observed *V*- and *K*-band images. The same wavelength dependence of the seeing size should be reproduced by uncorrected case of the GLAO simulations. A comparison between the *V*-band seeing through the Subaru Telescope and the outside seeing is also presented for evaluation of the dome seeing.

2 Method

The observations were made by the Subaru Telescope located on Mauna Kea, using IRCS [15] with AO188 [16]. After the acquisition of a star, AO loop was closed with low gain to cancel the focus drift of the telescope and then stopped for seeing measurement. The *V*-band ($0.55 \mu\text{m}$) images were obtained by the acquisition camera in the high-order WFS [17] in AO188 with the aperture of 20 arcsec in diameter and the *K*-band ($2.2 \mu\text{m}$) data by IRCS, synchronously. The pixel scale was 20 mas/pixel for the *V*-band, and 20 or 52 mas/pixel for the *K*-band. The observed stars are listed in Table 1. In the table, the *B*- and *R*-band magnitude are B2 and R2 mag, in the USNO-B1.0 catalog, respectively, and the *K*-band magnitude is taken from 2MASS catalog, checked up by VizieR² service. Because the *V*-band magnitude is not in the original catalogs, that in SIMBAD³ database is shown as reference, if available.

²<http://vizier.u-strasbg.fr/viz-bin/VizieR>.

³<http://simbad.u-strasbg.fr/simbad/>.

The observations were made on four nights by trying various settings as listed in Table 2. One sequence consists of five exposures. The number of frames in the 2nd column is less than five when the sequence was interrupted or some frames were excluded for analysis due to bad conditions. The star position was shifted on the detectors during a sequence along the dithering pattern shown in the 7th column. The mark 'X' or '+' following the dithering width shows the direction of the shift from the center (first) position. The dithering width is the separation of each position from the center position. Because the width is defined along the pixel grid, the actual distance from the center is $\sqrt{2}$ times larger in the case of 'X'. The star ID in the 4th column is the same as in Table 1. All of the observations were made at zenith angle between 20 deg and 30 deg as in the 5th column. The 6th column shows the exposure time. The standard was 60 sec, but was changed to 45 sec or 90 sec to adjust the signal level. Note that, in the seventh and eighth sets, the exposure time of the *K*-band images were 48 sec. This was because the co-add function of IRCS was used to avoid saturation without ND. The duration of the integration time including the overhead due to the co-add was adjusted to be 90 sec, i.e., the same as the exposure time of the *V*-band image. The last column shows imaging mode of IRCS: 20 mas or 52 mas and with or without an ND filter. For the first three nights, the synchronization of the *V*-band and the *K*-band was done manually. On the fourth night, all the dithering and exposures in the sequences were automatically performed by a script in the telescope observing system, which was quite efficient for data acquisition.

Table 2 Observation parameters of the obtained data

Set ID	# of Frame	Date (UT)	Star ID	θ_z [deg]	Exp.T. [sec]	Dither Pattern	<i>K</i> -band Mode
1	5	2013/01/12	1	22	60	5'' X	52ND
2	5			23	60	3'' X	52ND
3	5			24	60	3'' X	52ND
4	4		2	21	45	1.5'' X	52ND
5	5			22	45	1.5'' X	52ND
6	4	2013/01/25	3	21	60	1.5'' X	52ND
7	1	2013/05/21	4	21	90(K48)	1.5'' X	20
8	5			21	90(K48)	1.5'' X	20
9	4			21	90	1.5'' X	20ND
10	2	2014/03/20	5	25	60	2'' +	20ND
11	5		6	29	60	2'' +	20ND
12	5		7	26	60	2'' +	20ND
13	5		8	28	60	2'' +	20ND
14	5			28	60	2'' +	20ND
15	5		9	28	60	2'' +	20ND
16	5			29	60	2'' +	20ND
17	5		10	29	60	2'' +	20ND

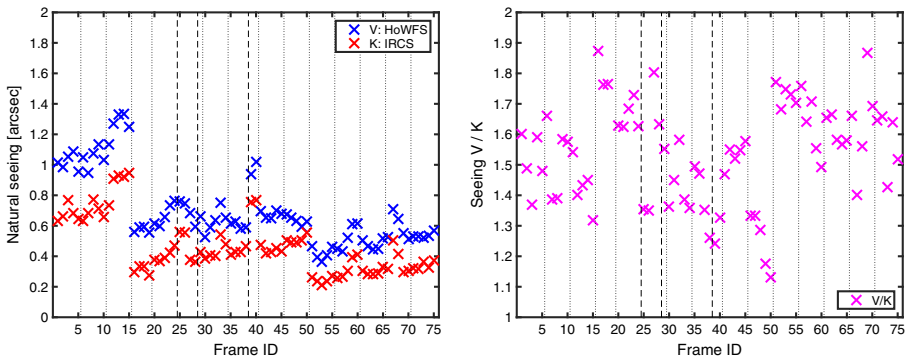


Fig. 1 Simultaneously obtained V -band and K -band FWHM, plotted along the frame number sequence in the left panel. The zenith angle dependence of the seeing is corrected. The right panel shows the ratio of the FWHM in the two bands

For the simultaneous observation in the two bands, there are constraints on the target star. To keep the exposure time constant, the brightness of the star should be also constant. In addition, the color of the star must be taken into account to adjust the counts in both V - and K -band images adequately. Also enough stars satisfying the condition must be available on the sky in a specific range of the zenith angle. Among the sequences shown in Table 1, the last three were the best condition, namely, $R \sim 10.0$ and $B - R \sim 1.0$ and observing by 20 mas mode of IRCS with an ND filter. The conditions can be used as a standard for further observations in future, though slight adjustment may be needed based on the seeing condition.

3 Results

The obtained data were reduced using IRAF⁴ software packages. The median sky background level in the sequence of the K -band frames was subtracted. For the V -band frames, only constant bias level was subtracted because the sky background was negligible. Next, the sensitivity difference of pixels was corrected for both bands, dividing the frames by the flat calibration frame of each band. The FWHM was measured by Moffat profile fitting in 'imexam' command after fixing bad and hot pixels in each frame. The aperture for the peak-profile fitting of the star was set to $3.2''$ in diameter. An annular region with inner and outer radius of $2.0''$ and $2.2''$ surrounding the star was used as sky region for the fitting. The measured FWHM is corrected for zenith angle (θ_z) dependence by multiplying $\cos^{3/5} \theta_z$.

The zenith-angle corrected FWHM is plotted in Fig. 1. The left panel shows the FWHM in the V - and the K -bands in blue and red, respectively. The right panel is the ratio of the two (i.e., the conversion factor we need). In these figures, the abscissa

⁴IRAF is distributed by the National Optical Astronomy Observatories, which are operated by the Association of Universities for Research in Astronomy, Inc., under cooperative agreement with the National Science Foundation.

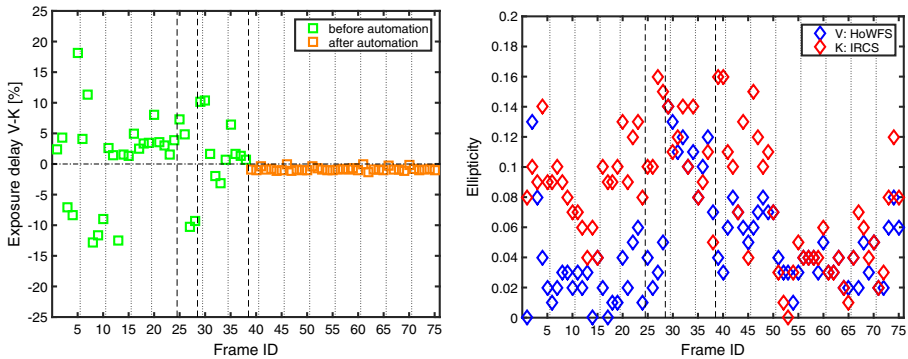


Fig. 2 The variation of observation parameters. The left panel shows the delay of the K -band exposure from the beginning of the V -band exposure, normalized by the V -band exposure time. The right panel shows the ellipticity of the peak profile of FWHM fitting

is the frame ID through all observed data in Table 2. The black dashed-lines and the dotted-lines show the change of the date and the sequence in Table 2, respectively. Note that, the frame ID is along the time sequence, but the interval is not equal. For example, the abrupt change of FWHM between the frame ID 15 and 16 was due to an interruption of observation due to high humidity for 3.5 hours. Also when the target star was changed, the overhead was a few minutes or more. As expected, the K -band seeing was better than the V -band seeing. The average of the ratio with the standard deviation is 1.54 ± 0.17 .

The delay of the exposure start-time and the ellipticity of the FWHM fitting are also plotted in Fig. 2 along the frame ID in the left and right panel, respectively. The delay of the K -band exposure from the beginning of the V -band exposure is plotted in the left panel by normalizing with the V -band exposure time. The delay scattered for the first three days, because the synchronization was done manually. Thanks to the automated script, the delay was small and constant for the last day. The delay time for data used here is within $\pm 20\%$. Three measurement points with the delay out of the range were removed from the data set and not included in Table 2. Three other measurement points having the ellipticity larger than 0.2 in the K -band were also removed from Table 2. The influence of these parameters on the conversion factor is discussed in the next section.

4 Discussion

4.1 Influence of observation parameters on the conversion factor

First, the influence of the delay between exposure time in the V - and the K -bands is examined. The conversion factor is plotted against the exposure delay in the left panel of Fig. 3. Because there is no clear tendency in the figure, the time delay less than 20% of the exposure time does not affect the measurement of the conversion factor seriously. Next, the influence of the ellipticity of the observed images is examined.

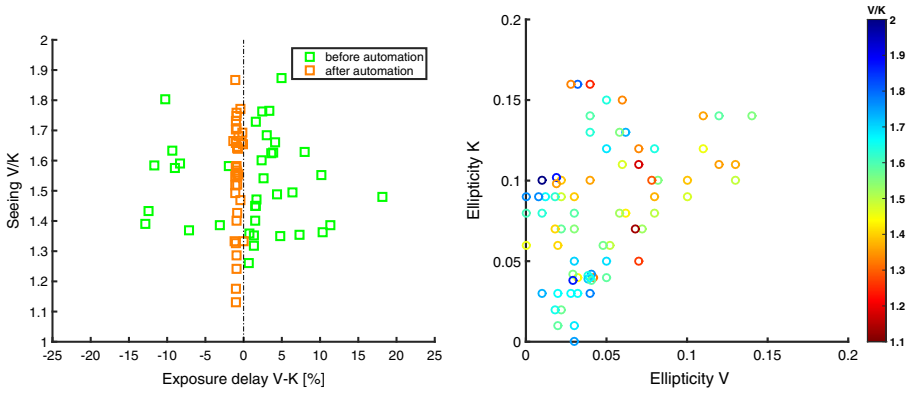


Fig. 3 The variation of the conversion factor (the ratio of seeing sizes between the *V*- and the *K*-bands). The left panel is plotted against the normalized delay time of the *K*-band exposure from the *V*-band. The right panel plots the ellipticities of the *V*- and the *K*-bands, color coded by *V*/*K* ratio. Overlapped points are plotted with slight offset to show the color clearly

The ellipticity of the *V*- and the *K*-bands are plotted in the right panel of Fig. 3. The plotted points are color-coded by the conversion factor. The ellipticity of the *K*-band is usually larger than that in the *V*-band (i.e., the points scatter in the upper left triangle on the right panel of Fig. 3), because the images are sharper and slight elongation is more prominent in the *K*-band. Therefore, FWHM in the *K*-band is affected more by the ellipticity than that in the *V*-band, so that *V*/*K* tends to be decreased. The ellipticity is brought due to slight offset of deformable mirror (DM) shape from the perfect flat at the seeing measurement. A useful practice to reduce the offset is closing AO loop just before the seeing image acquisition and reducing the loop gain gradually to stop. The average of the DM voltage commands during the closed-loop operation over a few minutes usually gives a flat shape at the observation time (adopted in this paper from Set ID 13 of Table 2). The other parameters in Table 2 do not seem to have any clear influence.

4.2 The variation of the conversion factor with seeing

The conversion factor is plotted in Fig. 4 against the *V*-band seeing with points color-coded by the ellipticity in the *V*-band. The conversion factor appears to increase in good seeing condition, as expected for turbulence with von Kármán power spectrum. The wavelength dependence of the seeing in von Kármán case, $\epsilon_{VK}(\lambda)$, differs from that in the Kolmogorov case, $\epsilon(\lambda)$. The seeing of Kolmogorov turbulence is expressed by Fried parameter, $r_0(\lambda)$, as

$$\epsilon(\lambda) = 0.98 \frac{\lambda}{r_0(\lambda)}, \tag{1}$$

$$r_0(\lambda) \propto \lambda^{6/5}, \tag{2}$$

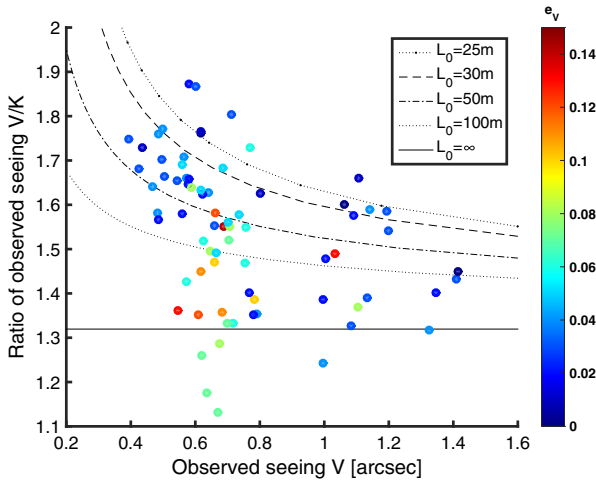


Fig. 4 The ratio of the observed V-band seeing to the observed K-band seeing is plotted against the observed V-band seeing. The expected ratios are overplotted for some values of the outer scale

where λ is the wavelength. The correction for the seeing of von Kármán turbulence is given by

$$\frac{\epsilon_{vk}(\lambda)}{\epsilon(\lambda)} = \sqrt{1 - 2.183 \left(\frac{r_0(\lambda)}{L_0}\right)^{0.356}}. \tag{3}$$

The (3) was obtained in [4] (19) as an approximation⁵ and used, for example, in [18]. From (3), the observed seeing ratio between the V- and the K-bands in von Kármán case is derived as

$$\frac{\epsilon_{vk}(V)}{\epsilon_{vk}(K)} = \frac{\epsilon(V)}{\epsilon(K)} \sqrt{\frac{1 - 2.183 \left(\frac{r_0(V)}{L_0}\right)^{0.356}}{1 - 2.183 \left(\frac{r_0(K)}{L_0}\right)^{0.356}}}. \tag{4}$$

By inserting relations:

$$\begin{aligned} \frac{\epsilon(V)}{\epsilon(K)} &= \frac{\lambda_V}{\lambda_K} \frac{r_0(K)}{r_0(V)} && \text{from (1),} \\ \frac{r_0(K)}{r_0(V)} &= \left(\frac{\lambda_K}{\lambda_V}\right)^{1.2} && \text{from (2),} \\ &\text{and} \\ \frac{\lambda_K}{\lambda_V} &= \frac{2.2}{0.55} = 4, \end{aligned}$$

⁵Although the FWHM in the relation is not obtained for Moffat fitting, the FWHM in this paper determined by Moffat fitting does not differ significantly from the direct measurement of the radial profile with no fitting.

Equation 4 is expressed as

$$\frac{V}{K} = 4^{0.2} \sqrt{\frac{1 - 2.183 \left(\frac{r_0(V)}{L_0}\right)^{0.356}}{1 - 2.183 \left(\frac{4^{1.2} r_0(V)}{L_0}\right)^{0.356}}}. \tag{5}$$

The expected curves of von Kármán power spectrum for various outer scale, L_0 , are overplotted on Fig. 4. The solid line ($L_0 = \infty$) corresponds to Kolmogorov power spectrum case ($V/K = 1.32$). The ellipticity of the V -band images is color code in the figure. The points with larger ellipticity seem to scatter around rather smaller conversion factor.

The outer scale is derived for each data point, with an assumption that the conversion factor is fully attributed to it. The left panel of Fig. 5 is a histogram of the outer scale. Only the physically likely range between 0 m and 160 m (53 out of the 75 samples) is plotted. The average and median of L_0 within the range are 53 m and 42m, respectively. These values are larger than typical value of 22 m at Cerro Paranal in Chile obtained by [19], and even larger than 30 m often adopted in AO simulations. Fortunately, the observed smaller conversion factor means more gain of GLAO at infrared wavelengths because the natural seeing becomes worse while the GLAO corrected image size little changes. Although the reason for the larger L_0 is still unclear only by this experimental result with limited number of samples, care has to be taken that small L_0 in an AO simulation could overestimate the conversion factor (i.e., underestimate the infrared seeing and the GLAO gain).

The right panel of Fig. 5 plots the ratio of observed raw seeing to the L_0 corrected seeing size (Kolmogorov; i.e., would be measured by a seeing monitor with small enough aperture than L_0) in the V -band (blue) and the K -band (red). The averages of the correction with standard deviations are 0.87 ± 0.06 in the V -band, and 0.74 ± 0.12 in the K -band. The data points with negative L_0 corresponding $V/K < 1.32$

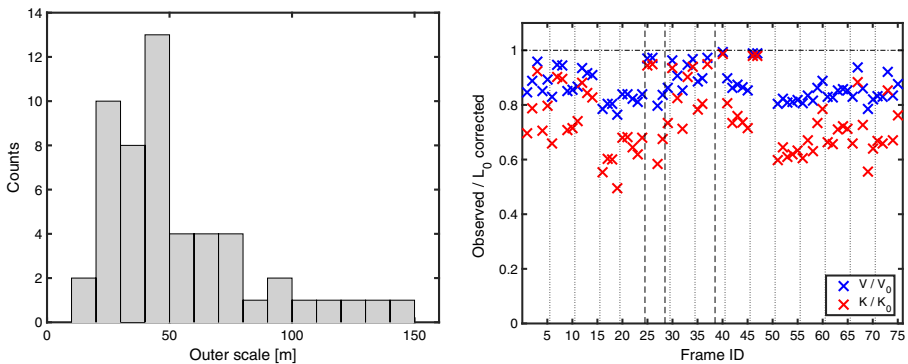


Fig. 5 The outer scale corresponds to the conversion factor. In the left panel, the histogram of the outer scale between 0 m and 160 m is shown. The right panel plots the ratio of measured raw seeing to the outer scale corrected (Kolmogorov) seeing in the V - and the K -bands. Points with the conversion factors which cannot be explained by even infinite outer scale are omitted in both figures

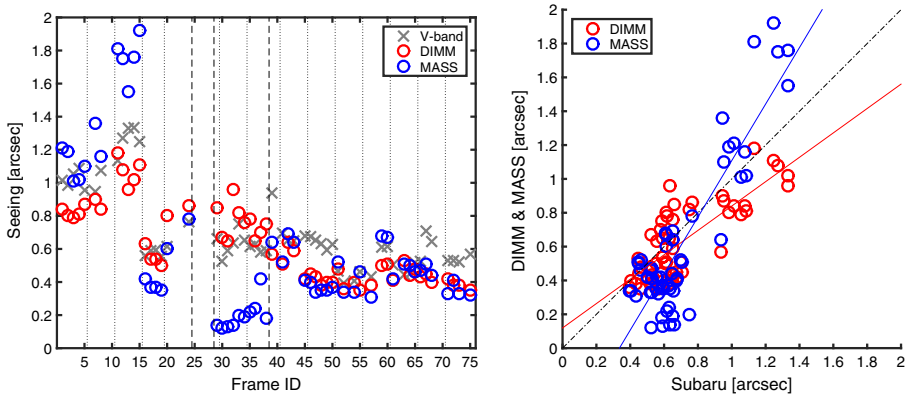


Fig. 6 The comparison of MASS-DIMM measurement on the Mauna Kea ridge site with the seeing through the Subaru Telescope. In the left panel, the seeing at $0.5 \mu\text{m}$ obtained by MASS and DIMM is plotted along the frame ID, together with the V-band seeing through the Subaru Telescope. The right panel plots MASS and DIMM against the V-band seeing. The dash-dot line is diagonal (the values on the abscissa and ordinate match)

in Fig. 4, are removed from Fig. 5 and the statistical values derived here. Also note that L_0 derived here is not necessarily purely atmospheric, but an 'effective' value including all effects affecting V/K ratio.

4.3 Comparison with outside seeing data

The seeing condition on Mauna Kea is monitored by using MASS-DIMM [4] and the data are available on MKWC website.⁶ When concurrent data exist during the exposure time of our images, the data are plotted together in Fig. 6. For MASS seeing, the value listed in the MASS profile table is adopted. The left panel is along frame ID together with the V-band seeing and the right panel is along the V-band seeing. Linearly fitted lines are also plotted. The intercept of the fitted line on the horizontal axis for MASS seeing is expected due to the lack of ground-layer component in the data. The seeing measured through the Subaru Telescope would show better figure, because the seeing measured by MASS-DIMM is considered as Kolmogorov spectrum, while the seeing measured through the Subaru Telescope is von Kármán spectrum affected by the outer scale as in (3). Moreover, at Very Large Telescope (VLT), the seeing through the telescope is better by about $0.15''$ than that measured by outside DIMM because the most of ground-layer seeing ($70 \sim 80\%$) concentrates below the telescope floor height of VLT (20m) and is not seen by the telescope [20]. On the contrary, the seeing through the Subaru Telescope is rather worse as in Fig. 6, except at some points.

The most plausible interpretation is that the seeing through the Subaru Telescope is affected by dome seeing. The amount of the dome seeing is estimated by subtracting DIMM seeing from that measured through Subaru Telescope. Note that the

⁶<http://mkwc.ifa.hawaii.edu/index.cgi>.

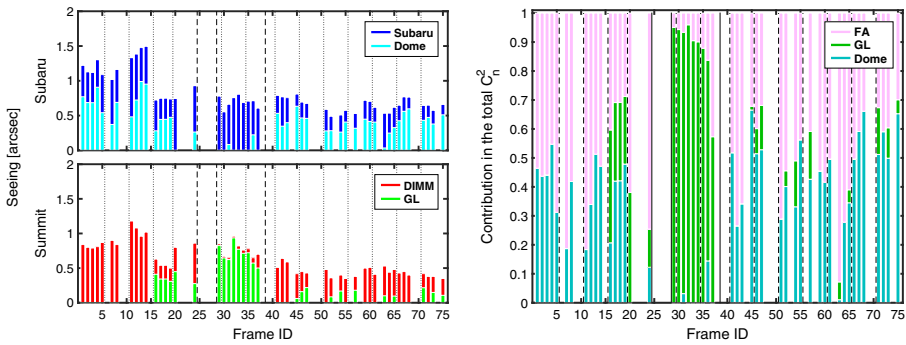


Fig. 7 Seeing components are compared in the left panel. The upper panel plots the dome component over the Subaru seeing and the lower panel plots the ground-layer (GL) component over the DIMM seeing. The right panel indicates the contribution of the free atmosphere (FA), ground-layer and the dome seeing in the total seeing of the Subaru Telescope. The Subaru data is corrected for the outer scale and the wavelength to $0.5 \mu\text{m}$. Only positive value is plotted in this figure

dome seeing mentioned here includes various effects: mirror seeing, the topographical difference between the Subaru Telescope site and the summit ridge site where MASS-DIMM is installed, and so on. Before the subtraction, the V -band seeing was converted to the Kolmogorov seeing at $0.5 \mu\text{m}$, using (1)–(3) with L_0 determined in the previous section from the conversion factor (the ratio of FWHM in the V -band to that in the K -band). The subtraction is done in terms of the turbulence strength, C_N^2 , taking the power law dependence of seeing on it with exponent of $3/5$ ($\epsilon \propto C_N^2 3/5$) into account as in [21].

The dome seeing and Subaru seeing at $0.5 \mu\text{m}$ are plotted in the upper left panel in Fig. 7. The ground-layer seeing was also calculated as the difference between DIMM and MASS seeing in terms of C_N^2 as in [21], and plotted in the lower left panel in Fig. 7 together with DIMM seeing. Note that negative value was not shown in the figures for both of the dome and the ground-layer seeing. Although the negative value is unphysical for the ground-layer, but not necessarily for the dome seeing. As mentioned above, the negative dome seeing would occur when the ground-layer seeing concentrates below the telescope floor height and is not seen by the telescope (the negative dome seeing value can be seen in the right panel of Fig. 8).

The contribution of each seeing component: dome, ground-layer and free upper atmosphere (MASS seeing) in the total seeing, is indicated in the right panel of Fig. 7. In the figure, the negative value of both dome and ground-layer components is treated as zero⁷. The average contributions of the dome seeing, ground layer, free atmosphere are 0.34, 0.21, 0.45 with standard deviations of 0.21, 0.33, 0.22, respectively. The contribution from the dome seeing is non-negligible part of the seeing through the

⁷The non-negative treatment is identical to define as follows: (i) The outside seeing is the DIMM seeing. When $\text{MASS} > \text{DIMM}$, MASS seeing is regarded as an error. (ii) The total seeing is the Subaru seeing. When $\text{DIMM} > \text{Subaru}$, free-atmosphere seeing is derived by multiplying MASS/DIMM ratio to the Subaru seeing.

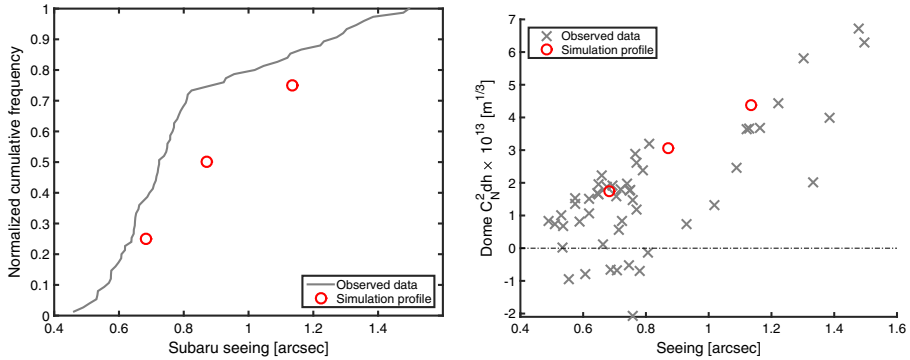


Fig. 8 Data used in the simulation profile (good, moderate, bad seeing conditions) are overplotted on the seeing data observed through the Subaru Telescope

Subaru Telescope, though the large standard deviation means the contribution from each component changes with the condition of the observing night. A merit of the ground-layer adaptive optics is correcting not only the ground-layer turbulence, but also the dome seeing, namely, about the half of the total seeing. Because the contribution of the dome component is usually large in the seeing through the Subaru Telescope, it should be reminded again that L_0 obtained in the preceding section is effective value rather than purely atmospheric.

The difference between the Subaru seeing statistics⁸ and an outside seeing campaign [22] at Thirty-Meter-Telescope (TMT) site (13N) was pointed out by [11] and added to the profile as a turbulence layer at 0 m in the simulation. The same procedure was adopted for Subaru GLAO simulation in [13]. The turbulence at 0 m can be considered as the dome seeing discussed in this section because the derivation is the same. Note that the dome seeing assumed in the simulation is based on the statistics of the large number of samples, but not synchronously obtained.

Figure 8 compares the observed seeing condition in this paper with that adopted in a simulations [13]. The left panel is the normalized cumulative frequency of the seeing condition, which indicates that the observed data (gray solid line) contain better seeing condition more than that adopted in the simulation (red circles: good, moderate, bad seeing conditions) based on the statistics of the large number of samples obtained by the longer-term monitoring. In the right panel of Fig. 8, the dome seeing component in the simulation (red circles) is overplotted on the observed data (gray crosses). The points seem to be within the range of observed data, though they are close to the upper boundary of the scattering range of the observed points. In [11, 13], the turbulence profile is derived combining two separately obtained statistics at TMT 13N [22] and the Subaru statistics regardless of simultaneity. Our result obtained here supports that the derived figures are in realistic range, though the sample is still limited and the seeing distribution is not exactly same.

⁸<http://www.naoj.org/Observing/Telescope/ImageQuality/Seeing/>.

5 Conclusion

We measured seeing in the V - and the K -bands simultaneously through the Subaru Telescope to evaluate the wavelength dependence of the seeing. The seeing was determined by the full-width at the half-maximum of a single star as usual in astronomical observations. The drift of the telescope focus was canceled by the closed-loop operation of adaptive-optics just before the measurement sequence. In total, 75 points of the measurement were obtained.

The overall average of the conversion factor, the ratio of the V -band seeing to the K -band seeing, was 1.54 ± 0.17 . The seeing calculation by performance simulation of an adaptive optics system, especially that for ground-layer adaptive optics, should be consistent with the observed distribution of the conversion factor. The conversion factor decreases as seeing size increases, as expected if the ratio is determined by the outer scale. Assuming that the ratio is purely determined by outer scale and using the empirical relation in [4], the distribution of the conversion factor is explained by the outer scale of ~ 50 m. The delay less than 20 % of the exposure between the two bands does not affect the measurement result of the conversion factor. On the other hand, larger ellipticity tends to result a smaller conversion factor (i.e., lower L_0). Therefore, the conversion factor obtained by this method should be considered as a lower limit, or an upper limit for the outer scale size.

The V -band seeing was converted to $0.5 \mu\text{m}$, and then compared with the outside seeing obtained by MASS-DIMM at the same time. The dome seeing contribution at the Subaru Telescope was estimated to be 34 % on average. The distribution of the dome seeing component against the total seeing is consistent with that adopted for Subaru GLAO simulation. The introduction of the dome seeing in the simulation based on the statistics of the large number of samples, but not obtained concurrently, was validated by the simultaneously-observed data in this paper.

These observational facts are found in still limited number of samples. Further data gathering with this method is desirable to draw more statistical conclusion.

Acknowledgments We would like to thank all staff of Subaru Telescope, National Astronomical Observatory, Japan, who kindly support our research. This work was inspired by the research supported by JSPS KAKENHI 24654050.

References

1. Fried, D.L.: *J. Optic. Society of America* **56**, 1372 (1966)
2. Kornilov, V., Tokovinin, A., Shatsky, N., Voziakova, O., Potanin, S., Safonov, B.: *Mon. Not. R. Astron. Soc.* **382**, 1269 (2007)
3. Roddier, F.: *Adaptive optics in astronomy* (Cambridge University Press) (1999)
4. Tokovinin, A.: *Publ. Astron. Soc. Pacific* **114**, 1156 (2002)
5. Martinez, P., Kolb, J., Tokovinin, A., Sarazin, M.: *Astron. Astrophys.* **516**, A90 (2010)
6. Tokovinin, A.: *Publ. Astron. Soc. Pacific* **116**, 941 (2004)
7. Rigaut, F.: *Beyond Conventional Adaptive Optics, ESO Conference and Workshop Proceedings* vol. 58. In: Vernet, E., Ragazzoni, R., Esposito, S., Hubin, N. (eds.) (2002). *ESO Conference and Workshop Proceedings*, 58, 11–16

8. Hayano, Y., Akiyama, M., Hattori, T., Iwata, I., Kodama, T., Lai, O., Minowa, Y., Ono, Y., Oya, S., Takiura, K., Tanaka, I., Tanaka, Y., Arimoto, N.: Adaptive Optics Systems IV, Proc. SPIE, vol. 9148. In: Marchetti, E., Close, L.M., Véran, J.P. (eds.) (2014). Proc. SPIE, 9148, 2S.1–2S.8
9. Andersen, D.R., Stoesz, J., Morris, S., Lloyd-Hart, M., Crampton, D., Butterley, T., Ellerbroek, B., Jolissaint, L., Milton, N., Myers, R., Szeto, K., Tokovinin, A., Véran, J.P., Wilson, R.: Publ. Astron. Soc. Pacific **118**, 1574 (2006)
10. Wang, L., Andersen, D., Ellerbroek, B.: Appl. Opt. **51**, 3692 (2012)
11. Andersen, D.R., Jackson, K.J., Blain, C., Bradley, C., Correia, C., Ito, M., Lardière, O., Véran, J.P.: Publ. Astron. Soc. Pacific **124**, 469 (2012)
12. Oya, S., Akiyama, M., Hayano, Y., Minowa, Y., Iwata, I., Terada, H., Usuda, T., Takami, H., Nishimura, T., Kodama, T., Takato, N., Tomono, D., Ono, Y.: Adaptive Optics Systems III, Proc. SPIE, vol. 8447. In: Ellerbroek, B.L., Hart, M., Hubin, N., Wizinowich, P.L. (eds.) (2012). Proc. SPIE, 8447, 3V.1–3V.11
13. Oya, S., Hayano, Y., Lai, O., Iwata, I., Kodama, T., Arimoto, N., Minowa, Y., Akiyama, M., Ono, Y.H., Terada, H., Usuda, T., Takami, H., Nishimura, T., Takato, N., Tomono, D.: Adaptive Optics Systems IV, Proc. SPIE, vol. 9148. In: Marchetti, E., Close, L.M., Véran, J.P. (eds.) (2014). Proc. SPIE, 9148, 6G.1–6G.8
14. Ziad, A., Maire, J., Borgnino, J., Dali Ali, W., Berdja, A., Ben Abdallah, K., Martin, F., Sarazin, M.: Adaptive Optics for Extremely Large Telescopes, AO4ELT conference, vol. 1. In: Clénet, Y., Conan, J.M., Fusco, T., Rousset, G. (eds.) (2010). AO4ELT conference, 1, 03008
15. Kobayashi, N., Tokunaga, A., Terada, H., Goto, M., Weber, M., Potter, R., Onaka, P.M., Ching, G.K., Young, T.T., Fletcher, K., Neil, D., Robertson, L., Cook, D., Imanishi, M., Warren, D.W.: Optical and IR Telescope Instrumentation and Detectors, Proc. SPIE, vol. 4008. In: Iye, M., Moorwood, A. (eds.) (2000). Proc. SPIE, 4008, 1056–1066
16. Watanabe, M., Takami, H., Takato, N., Colley, S., Eldred, M., Kane, T., Guyon, O., Hattori, M., Goto, M., Iye, M., Hayano, Y., Kamata, Y., Arimoto, N., Kobahashi, N., Minowa, Y.: Advancements in Adaptive Optics, Proc. SPIE, vol. 5490. In: Calia, D.B., Ellerbroek, B.L., Ragazzoni, R. (eds.) (2004). Proc. SPIE, 5490, 1096–1104
17. Watanabe, M., Oya, S., Hayano, Y., Takami, H., Hattori, M., Minowa, Y., Saito, Y., Ito, M., Murakami, N., Iye, M., Guyon, O., Colley, S., Eldred, M., Golota, T., Dinkins, M.: Adaptive Optics Systems, Proc. SPIE, vol. 7015. In: Hubin, N., Max, C.E., Wizinowich, P.L. (eds.) (2008). Proc. SPIE, 7015, 64.1–64.8
18. Martinez, P., Kolb, J., Sarazin, M., Tokovinin, A.: ESO Messenger **141**, 5 (2010)
19. Martin, F., Conan, R., Tokovinin, A., Ziad, A., Trinquet, H., Borgnino, J., Agabi, A., Sarazin, M.: Astron. Astrophys. Suppl. Ser **516**, A90 (2010)
20. Sarazin, M., Melnick, J., Navarrete, J., Lombardi, G.: Seeing Clearly. In: Businger, S., Cherubini, T. (eds.) (Virtualbookworm.com Publishing Inc., 2011), chap. 5, 89–99
21. Skidmore, W., Els, S., Travouillon, T., Riddle, R., Schöck, M., Bustos, E., Seguel, J., Walker, D.: Publ. Astron. Soc. Pacific **121**, 1151 (2009)
22. Els, S.G., Travouillon, T., Schöck, M., Riddle, R., Skidmore, W., Seguel, J., Bustos, E., Walker, D.: Publ. Astron. Soc. Pacific **121**, 527 (2009)